Phase transition pathway of hybrid halide perovskites under compression: Insights from first-principles calculations

Dongwen Yang,[1,2,*] Yuhao Fu,[3,*] Yuanhui Sun,[1] Yawen Li,[1] Kai Wang,[4] Zewen Xiao,[5] Koushik Biswas,[6,†] and Lijun Zhang[1,‡]

[1]*State Key Laboratory of Superhard Materials, Key Laboratory of Automobile Materials of MOE, and School of Materials Science, Jilin University, Changchun 130012, China*

[2]*Key Laboratory of Materials Physics of Ministry of Education, School of Physics and Microelectronics, Zhengzhou University, Zhengzhou 450052, China*

[3]*State Key Laboratory of Superhard Materials, College of Physics, Jilin University, Changchun 130012, China*

[4]*State Key Laboratory of Superhard Materials, Jilin University, Changchun 130012, China*

[5]*Wuhan National Laboratory for Optoelectronics, Huazhong University of Science and Technology, Wuhan 430074, China*

[6]*Department of Chemistry and Physics, Arkansas State University, State University, Arkansas 72467, USA*

(Received 13 May 2020; revised 19 December 2020; accepted 12 April 2021; published 10 May 2021)

Lead halide perovskites undergo pressure-induced phase transition, facilitated by bond compressions and different tilt patterns of the PbI_6 octahedra. Utilizing first-principles calculations we investigated 14 possible tilt systems of $CH_3NH_3PbI_3$ under compression, derived from the high-symmetry $Pm\bar{3}m$ structure. Fr substitution is adopted to mimic the rotational disorder effect of the CH_3NH_3 cation with the similar size (at room temperature or higher). Analyses of these phases reveal an interplay between tilting and distortion of the PbI_6 octahedra. Dynamical fluctuations at finite temperature provide additional insight into the phases' stability. Drawing from the trends observed in $FrPbI_3$ and additional calculations for perovskites involving differently ordered organic cations, we propose that phase transition in $CH_3NH_3PbI_3$ occurs from tetragonal at ambient pressure to orthorhombic under high pressure via the pathway $I4/mcm \rightarrow P4/mbm \rightarrow Imm2$. The distinct discontinuity in the calculated volume-pressure curve of $I4/mcm$ and band-gap evolution of the proposed phases are consistent with photoluminescence shifts observed in $CH_3NH_3PbI_3$ under pressure.

DOI: 10.1103/PhysRevMaterials.5.054603

I. INTRODUCTION

In a few short years, lead halide perovskites have distinguished themselves as one of the leading contenders in emerging photovoltaics technology. Latest reports suggest a certified power conversion efficiency (PCE) in excess of 25% on devices built from these materials [1–3]. Such rapid improvement in PCE is attributed to the superior properties of lead halide perovskites, such as high optical absorption coefficient, moderate-to-low effective mass of electrons and holes, long diffusion length, and lifetime of photogenerated carriers, low trap densities, and weak exciton binding energy [4–10]. They can even be synthesized via low-temperature solution processes. All of these advantages have stimulated a surge in research activity aimed at understanding their fundamental properties and finding ways to optimize them, so as to suit the needs of different optoelectronic applications, including solar cells [11–19].

Applying pressure to a material can induce structural changes to alter and tune its electronic and optical properties [20,21]. The response of lead halide perovskites under compression is therefore a subject of considerable interest. Piezochromic transitions under pressure have been observed in several hybrid perovskites, which signal changes in the fundamental gap and electronic structure. It is likely caused by phase transitions initiated by octahedral rotations and bond contractions under pressure. Jaffe *et al.* reported the orthorhombic structure ($Fmmm$) of $CH_3NH_3PbI_3$ ($MAPbI_3$) transformed to a cubic phase ($Im\bar{3}$) at a pressure ~0.3 GPa and amorphization ensued above 2.7 GPa [22,23]. Jiang *et al.* illustrated $MAPbI_3$ undergoes two high-pressure phase transformations from a tetragonal structure ($I4/mcm$) at ambient condition to a cubic phase ($Im\bar{3}$) at 0.3 GPa, then to a putative orthorhombic $Immm$ structure at 2.7 GPa [24]. Other reports describe $MAPbI_3$ transitions from tetragonal structure ($I4/mcm$) at ambient pressure to an orthorhombic structure ($Imm2$) at ~0.3 GPa and amorphization onset above 2 GPa [25,26]. It is notable that the cubic or orthorhombic structures reported under moderate pressure of about 0.3 GPa [22–26] feature distinct octahedral tilt patterns in addition to different crystal symmetry. Even under ambient conditions, $MAPbI_3$ structure has been reported in different tetragonal and orthorhombic space groups, e.g., $I4cm$ [27], $I4/mcm$ [24–26,28], and $Fmmm$ [22]. The disagreements possibly stem from complications associated with powder-diffraction or single-crystal diffraction experiments.

Proper identification of the actual phases under pressure and how they correlate with observed material properties is clearly a significant area, worthy of investigation

*These authors contributed equally to this work.
†kbiswas@astate.edu
‡lijun_zhang@jlu.edu.cn

TABLE I. ISOTROPY subgroups of $Pm\bar{3}m$ exhibiting rotations of octahedra given by irreps M_3^+ and R_4^- with order-parameter directions in parentheses. The lattice vectors and origin shifts are given with respect to high-symmetry $Pm\bar{3}$m structure [41].

Space group	Tilt pattern	M_3^+	R_4^-	Lattice vectors	Origin
$Pm\bar{3}m$ (221)	$a^0a^0a^0$	(0 0 0)	(0 0 0)	(100),(010),(001)	(0 0 0)
$I4/mcm$ (140)	$a^0a^0c^-$	(0 0 0)	(0 0 c)	(110),($\bar{1}$10),(002)	(0 0 0)
$P4/mbm$ (127)	$a^0a^0c^+$	(0 0 c)	(0 0 0)	(110),($\bar{1}$10),(001)	(0 0 0)
$I4/mmm$ (139)	$a^0b^+b^+$	(0 b b)	(0 0 0)	(020),(002),(200)	(0.5 0.5 1.5)
$C2/m$ (12)	$a^0b^-c^-$	(0 0 0)	(0 b c)	(0$\bar{2}$0),(200),(011)	(0.5 0.5 0)
$Cmcm$ (63)	$a^0b^+c^-$	(0 b 0)	(0 0 c)	(200),(00$\bar{2}$),(020)	(0.5 0 0.5)
$Imma$ (74)	$a^0b^-b^-$	(0 0 0)	(0 b b)	(011),(200),(01$\bar{1}$)	(0 0 0)
$Im\bar{3}$ (204)	$a^+a^+a^+$	(a a a)	(0 0 0)	(200),(020),(002)	(0.5 0.5 0.5)
$R\bar{3}$c (167)	$a^-a^-a^-$	(0 0 0)	(a a a)	($\bar{1}$10), (0$\bar{1}$1),(222)	(0 0 0)
$P\bar{1}$ (2)	$a^-b^-c^-$	(0 0 0)	(a b c)	(011),(101),(110)	(0 0 0)
$Immm$ (71)	$a^+b^+c^+$	(a b c)	(0 0 0)	(200),(020),(002)	(0.5 0.5 0.5)
$C2/c$ (15)	$a^-b^-b^-$	(0 0 0)	(a b b)	(2$\bar{1}\bar{1}$), (01$\bar{1}$),(011)	(0.5 0.5 0)
$P4_2/nmc$ (137)	$a^+a^+c^-$	(a a 0)	(0 0 c)	(200),(020),(002)	(0 0 $\bar{1}$)
$P2_1/m$ (11)	$a^+b^-c^-$	(a 0 0)	(0 b c)	(0$\bar{1}$1),(200),(011)	(0 0 0)
$Pnma$ (62)	$a^+b^-b^-$	(a 0 0)	(0 b b)	(011),(200),(01$\bar{1}$)	(0 0 0)

among halide perovskites. The aim of this paper is a better understanding of the nature of the pressure-induced phase transformations in methylammonium (CH_3NH_3) hybrid halide perovskites. Using van der Waals (vdW) corrected density functional theory (DFT) calculations, we investigated the enthalpy evolution of all possible distorted systems of $FrPbI_3$ as a function of pressure at 0 K. Fr substitution is necessary to mimic the rotational disorder of the MA cation (at room temperature or higher). Based on an analysis of unique octahedral tilt patterns and corresponding enthalpy and phonon dispersion of $FrPbI_3$, we propose a pressure-induced phase transition pathway of $MAPbI_3$. Further investigation of the proposed $MAPbI_3$ phases reveals the nature of band-gap variation under compression, which correlates well with the reported experimental observations.

II. COMPUTATIONAL METHODS

The first-principles calculations are based on DFT using plane-wave pseudopotential approach as implemented in the Vienna *ab initio* simulation package (VASP) [29,30]. The electron-ion interactions are described via projector augmented-wave pseudopotentials with 1 s for H, $2s^22p^2$ for C, $2s^22p^3$ for N, $3s^23p^5$ for Cl, $4s^24p^5$ for Br, $5s^25p^5$ for I, $6s^26p^2$ for Pb, $6s^26p^67s$ for Fr as valence electrons [31], We used the Perdew, Burke, and Ernzerhof (PBE) parametrization of the generalized gradient approximation (GGA) as the exchange correlation functional [32]. Structural optimizations were done with a kinetic energy cutoff of 400 eV and Brillouin zone integration via k-point meshes of spacing $2\pi \times 0.03$ Å^{-1}. We optimized the equilibrium structural parameters (lattice parameters and internal coordinates) of $FrPbI_3$ including all structures presented in Table I and $MAPbI_3$ including tetragonal and orthorhombic structure through total energy minimization with the residual forces on the atoms converged to below 0.02 eV/Å. The tetragonal structure and orthorhombic structure with space group of $I4/mcm$ and $Imm2$ for $MAPbI_3$ are used to calculate the ground-state properties under ambient condition and under high pressure. The band structure and density of states of orthorhombic $Imm2$ structure are calculated with DFT-PBE functional. Pressure was applied by adding Pulay stress to the diagonal elements of the stress tensor. To properly take into account the long-range vdW interactions that play a sizable role in the hybrid perovskites involving organic molecules, we have calculated lattice constants of $MAPbI_3$ at different level of theory as shown in Table S1 in the Supplemental Material [33]. We found that OptB86b and D2 functionals both give satisfactory agreements with experimental lattice parameters. We choose the vdW-optB86b functional for our calculations [34,35].

The harmonic phonon dispersion of $FrPbI_3$ structure was calculated in $2 \times 2 \times 2$ supercell with a $3 \times 3 \times 3$ k-point mesh based on the finite displacement approach as implemented in PHONOPY [36]. The temperature-dependent phonon calculations were carried out using the temperature-dependent effective potential (TDEP) code as developed by Hellman *et al.* [37–39]. The harmonic and anharmonic (including the third- and fourth-order) force constants can be obtained by fitting the Born-Oppenheimer potential energy surface. The energy surface is sampled by using *ab initio* molecular dynamics (AIMD) at a finite temperature with the NVT ensemble. We used an 80-atom ($2 \times 2 \times 2$) supercell and 1-fs time step for the MD simulations. The MD calculations are performed at room temperature (300 K) in our work. We found the change of frequency of vertical axis with larger supercell is less than 0.034 THz as shown in Fig. S1 in the Supplemental Material [33]. The frequency of vertical axis almost keeps unchanged after considering the nonanalytical term correction (NAC) contributions as shown in Fig. S2 [33]. Notice the LO-TO splitting when nonanalytical contributions are included. The conclusions that summarized from phonon dispersions with smaller supercell and without LO-TO splitting are still held. For the Brillouin zone integration, we used a $1 \times 2 \times 2$ k-point mesh and Fermi smearing corresponding to the predefined simulation temperature. This method can provide accurate phonon dispersion relations and free energies for anharmonic systems. The transition barriers were calculated using nudged elastic band (NEB) method in conjunction

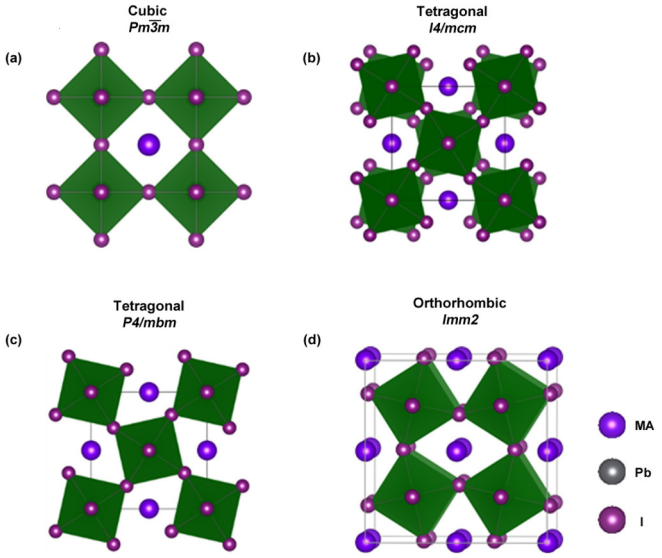

FIG. 1. (a)–(d) The four typical crystal structures observed in lead halide peorvskites with space group of $Pm\bar{3}m$, $I4/mcm$, $P4/mbm$, and $Imm2$.

with the climbing image method [40]. Crystal structures of all possible distorted systems presented in this paper were obtained with the aid of the program ISOTROPY [41].

III. RESULTS AND DISCUSSION

The APbX_3 halide perovskite structure (X = halogen ion) can be viewed as a three-dimensional framework of corner-connected $[PbX_6]^{4-}$ octahedra with A site cations occupying the cuboctahedral cages to stabilize the lead-halogen framework. The A cations could be monovalent organic [e.g., $CH_3NH_3^+$, $CH(NH_2)_2^+$] or inorganic (e.g., Cs^+, Rb^+) ion. At finite temperatures, APbX_3 perovskites exhibit three phases (α, β, γ) within four space groups, i.e., the cubic ($Pm\bar{3}m$), tetragonal ($I4/mcm$, $P4/mbm$), and orthorhombic ($Imm2$) phases as shown in Fig. 1. Taken $MAPbI_3$ as an example of hybrid perovskites, it adopts the cubic α phase with space group $Pm\bar{3}m$ at temperature above 330 K [Fig. 1(a)]. The MA cations in α phase are randomly orientated and the overall crystal preserves O_h symmetry [42–45]. The freedom of MA molecules in the room-temperature β phase is slightly reduced, but their orientations are still disordered. As the temperature lowers (∼165 K), the rotation of the MA cations is hindered [46]. The frozen MA molecules having fixed alignments lead to transformation from tetragonal β to orthorhombic γ phase with accompanying rotation and distortion of $[PbI_6]^{4-}$ octahedra.

The perovskite structure is a network of corner-sharing octahedra and there are several possibilities for tilts. The distorted perovskite phases can be obtainable from the cubic $Pm\bar{3}m$ aristotype by applying various tilt patterns to the corner-linked octahedra. The distortions allow changes in the lattice parameters and unit-cell size, afford flexibility in preferred coordination of the A-cation without drastically changing the octahedral bonding environment of Pb. Howard *et al.* performed group-theoretical analysis which yields 14 space groups derived through octahedral tilting [41]. The tilt patterns are mediated by the irreducible representations R_4^- and M_3^+ and their combination. All 14 unique tilt systems along with cubic $Pm\bar{3}m$ reference phase are presented in Table I. The calculated lattice parameters for $FrPbI_3$ at ambient condition are also shown in Table S2 in the Supplemental Material [33].

The stability of the tilt systems can be analyzed by the harmonic and anharmonic phonon spectra of the corresponding structures. For computational expediency, we circumvent the problem of calculating a large number $MAPbI_3$ supercell structures by replacing MA with Fr. We, of course, acknowledge that Fr is radioactive and $FrPbI_3$ is a hypothetical material. Using it as a virtual cation instead of Cs^+ could be advantageous because ionic radius of Fr^+ is larger than Cs^+ and closer to that of MA^+ as shown in Table S3 in the Supplemental Material [33]. Moreover, the Fr ion can reasonably mimic the rotational disorder effect of the MA cation at room temperature or higher. Goldschmidt's tolerance factor of $FrPbI_3$ is also closer to that of $MAPbI_3$ (Table S3 [33]). From the formula of tolerance factor t $[(r_{Fr} + r_I)/[\sqrt{2}(r_{Pb} + r_I)]$, one can see the t of $FrPbI_3$ does not change under high pressure.

It is true that the replacement of MA by Fr would ignore the effect of hydrogen bonding. However, we may still obtain trends and valuable insight which is our primary objective. In this context, it is important to mention that recent DFT calculations have shown that Fr provide a better accounting of the stability trend (compared to Cs) when used as a virtual ion in place of MA in hybrid double perovskites [47]. We found that the energies of $MAPbI_3$ and $FrPbI_3$ both are in the order of $E(\gamma) < E(\beta) < E(\alpha)$. Moreover, charge distribution of the rotationally disordered MA^+ at or above room temperature may be well described by Fr^+. We also note that our calculations show that the overall electronic structure of $FrPbI_3$, especially the band edges (derived from Pb 6s, 6p, and I 5p) are similar to that of $MAPbI_3$. For comparison, the density of states of $FrPbI_3$ and $MAPbI_3$ cubic structure are shown in Fig. S3 in the Supplemental Material [33].

Figures 2(a) and 2(b) present the calculated total energy difference (ΔH) of 14 possible tilt systems of $FrPbI_3$ under pressure (up to 3.0 GPa) relative to the cubic α phase at 0 K. The free energy of a structure is the sum of the internal energy (U) and the product of pressure and volume (PV) given by the equation: G=U+PV. It should be emphasized that in our work the free energies were calculated at zero temperature. Once the temperature effect is included, the free energy will include the contributions such as thermal expansion, lattice vibrations, entropy effect, etc. Saidi *et al.* found by first-principles calculations that the lattice vibration is the major contributing factor for stabilizing the cubic phase at room and high temperatures [46]. If the temperature effect is included, the energy order $[E(\gamma) < E(\beta) < E(\alpha)]$ would be changed and the α/β phases would be stabilized. In addition, Wright *et al.* reported the energy for the interacting longitudinal optical phonon modes and the Fröhlich coupling constants at room temperature in $MAPbI_3$ are 11.5 and 40 meV, respectively. It is demonstrated that the electron-phonon coupling in hybrid halide perovskites is dominated by Fröhlich coupling between charge carrier and longitudinal optical phonon modes [48]. Under compression, the intensity

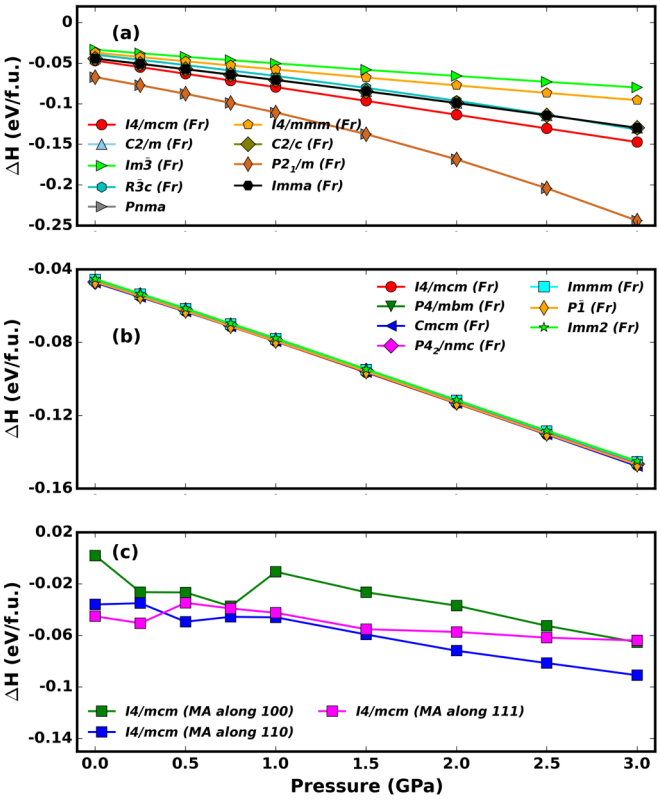

FIG. 2. (a) Calculated ΔH between distorted system and cubic ($Pm\bar{3}m$) phase of $FrPbI_3$ as a function of pressure. (b) Symbols corresponding to *Cmcm*, $P4_2/nmc$, *Immm*, $P\bar{1}$ structures overlap with that of $I4/mcm$ and $P4/mbm$ and thus shown separately. (c) ΔH between tetragonal ($I4/mcm$) and cubic $MAPbI_3$ with different MA orientations under changing pressure. All enthalpies are calculated by DFT-PBE method.

of interactions via Fröhlich coupling in $MAPbI_3$ may slightly increase because of the distortion of lattice. Due to the large energy difference (∼0.024 eV/f.u.) between tetragonal and orthorhombic phases at 0 K, the energy order might not be changed. Such calculations are beyond the scope of this study. With increasing pressure, the downward gradient of each plot represents improved stability of the corresponding structure with respect to the α phase. The enthalpies of cubic $Im\bar{3}$ structure with tilt pattern $a^+a^+a^+$ in Glazer notation are the highest (i.e., lowest magnitude of ΔH in Fig. 2(a) among all the distorted systems. The enthalpy of structures of space group $C2/m$, $R\bar{3}c$, $I4/mmm$, $C2/c$, *Imma* are located between cubic $Im\bar{3}$ and tetragonal $I4/mcm$. In addition, the energies of the structures of space group $P4/mbm$, *Cmcm*, $P4_2/nmc$, *Immm*, and $P\bar{1}$ are very close to that of tetragonal $I4/mcm$. Relative to $I4/mcm$, these structure are within 2 meV per formula unit. It is indicative of the ease of phase transformations among these structures. The orthorhombic *Pnma* structure and monoclinic $P2_1/m$ structure (with $a^+b^-b^-$ and $a^+b^-c^-$ tilt patterns) having the lowest energy are ground-state phases. We note that only $KCaF_3$ and $KMnF_3$ are reported to be monoclinic $P2_1/m$ structure in the inorganic crystal structure database (ICSD) [49].

In addition to the different $FrPbI_3$ tilt systems, we tested the impact of MA ion orientation (along 100, 110, 111 principal

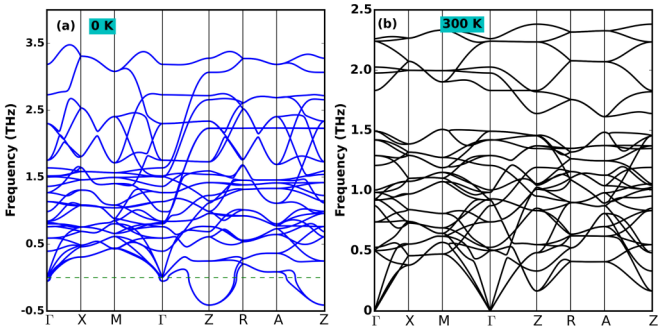

FIG. 3. The calculated phonon dispersion of tetragonal $P4/mbm$ structure using DFT-PBE method for $FrPbI_3$ at (a) 0 K and (b) at 300 K,respectively. The coordinates of high-symmetry K points are Γ (0, 0, 0), X (0, 0.5, 0), M (0.5, 0.5, 0), Z (0, 0, 0.5), R (0, 0.5, 0.5), A (0.5, 0.5, 0.5) [53].

axes) in tetragonal $MAPbI_3$ ($I4/mcm$, tilt pattern of $a^0a^0c^-$) under compression. The energy difference ΔH between the tilted structure and cubic α phase of $MAPbI_3$ follows the same general trend with increasing pressure as does $FrPbI_3$ [Fig. 2(c)]. However, as shown in Fig. S4 in the Supplemental Material [33], the total energy changes of $MAPbI_3$ are dependent on the orientation of the MA ions. This dependence may be attributed to different steric and hydrogen bonding effects caused by distinct MA orientations.

We further examine the dynamical stability of $FrPbI_3$ structures having space groups $I4/mcm$, $P4/mbm$, *Cmcm*, $P4_2/nmc$, *Immm*, and $P\bar{1}$. Their phonon dispersions at 0 and 300 K are shown in Figs S5 and S6, respectively [33]. Phonon dispersion of *Cmcm*, $P4_2/nmc$, *Immm* structures (Figs. S5c and S6a, S5d and S6b, S5e and S6c in the Supplemental Material [33]) exhibit imaginary optical modes in the Brillouin zone. We find small phonon instability in the $P4/mbm$ and $P\bar{1}$ structures near the Z point and L point, respectively. Among perovskite compounds, anharmonic effect is important in phonon calculations [50]. Indeed, when phonon-phonon interactions between Fr ions and their iodine cages at 300 K are taken into account, the imaginary modes of $P4/mbm$ and $P\bar{1}$ structures disappear as shown in Fig. 3(b) and Fig. S6d [33] in the Supplemental Material ([51,52]). It indicates that this structure may be dynamically stabilized under ambient conditions. However, the total energy of $P\bar{1}$ structure is higher than that of $P4/mbm$ for $MAPbI_3$. We anticipate the $P4/mbm$ structure can be stabilized under ambient conditions. The $I4/mcm$ structure exhibits imaginary modes at M and A points in the Brillouin zone as shown in Fig. S5a [33]. The displacement patterns of soft modes corresponding to M and A points and the partial density of states are shown Figs. S7 and S8 [33], respectively. One can see that the displacement of halide atoms contribute to the hardening of soft phonon modes.

To further evaluate the possibility of phase transformation from $I4/mcm$ to $P4/mbm$, we calculated the transition barrier of $FrPbI_3$ as shown in Fig. 4. We also calculated the transition barrier from $I4/mcm$ to *Imm2* for comparison. The transition barrier from $I4/mcm$ to *Imm2* is 396 meV at atmospheric pressure, which is significantly higher than that of phase transformation from $I4/mcm$ to $P4/mbm$. The transition

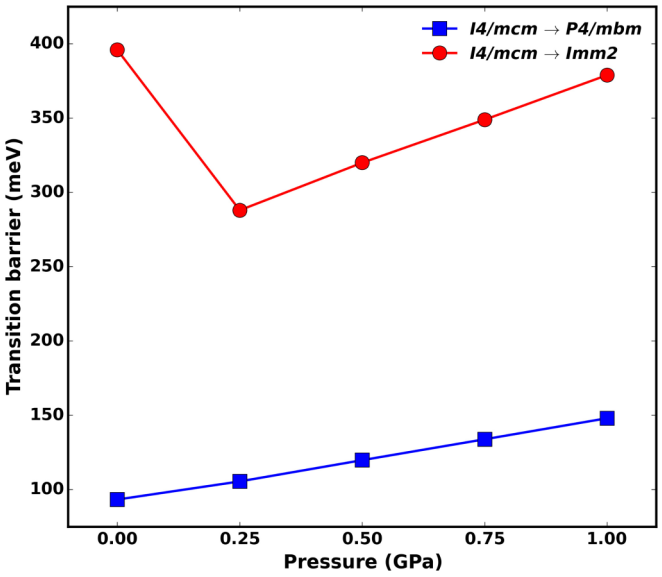

FIG. 4. Calculated transition barrier of $FrPbI_3$ from $I4/mcm$ to $P4/mbm$ (blue line) and $I4/mcm$ to $Imm2$ (red line) structure as a function of pressure using NEB method.

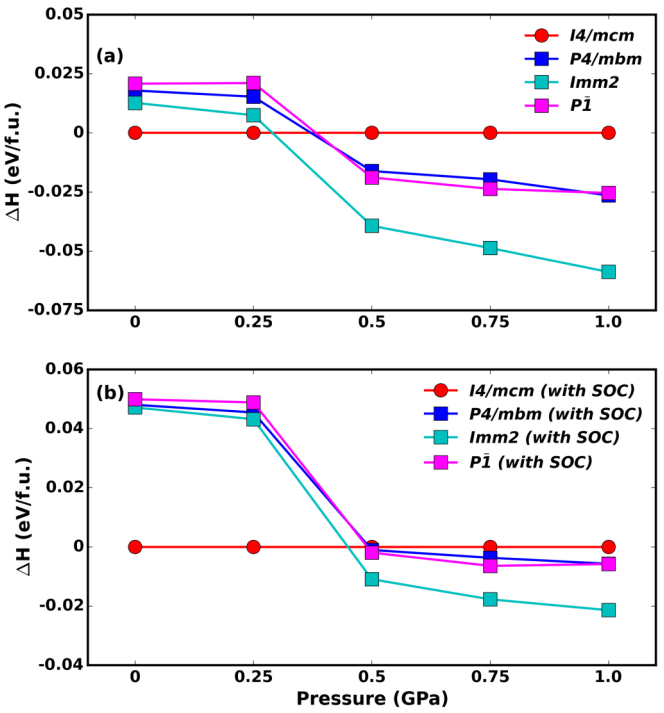

FIG. 5. Enthalpy difference of tetragonal $P4/mbm$, orthorhombic $Imm2$, and triclinic structure relative to tetragonal $I4/mcm$ structure of $MAPbI_3$ (a) without SOC (b) with SOC as a function of pressure. The enthalpies are calculated by DFT-PBE method. The principal axes of MA molecule oriented to the [111] direction.

barrier from $I4/mcm$ to $Imm2$ decreases until 0.25 GPa and then increases gradually with pressure. While the transition barrier from $I4/mcm$ to $P4/mbm$ increases gradually under pressure. The increasing barrier height may be attributed to reduced lattice constant and volume contraction under pressure. We thus inferred that the existence of intermediate phase ($P4/mbm$) can significantly reduce the transition barrier from $I4/mcm$ to $Imm2$. We also have analyzed the phase transition from $I4/mcm$ to $P4/mbm$ using group theory. The tetragonal phase with space group $P4/mbm$ is a subgroup of the tetragonal phase with space group $I4/mcm$. According to group theory, the space group $I4/mcm$ can go to $P4/mbm$ via M_3^+ transformation [54]. The operation of M_3^+ leads to the correct atomic positions: $(y-\frac{1}{2}, -x+\frac{1}{2}, -\frac{2}{3}z+\frac{1}{2})$ in the $P4/mbm$ phase, where (x, y, z) are the reduced coordinates of an atom in the $I4/mcm$ phase. Accordingly, the Fr atoms at 4b (Wyckoff) positions (0.0, 0.5, 0.75) in the $I4/mcm$ phase transform to the 2d positions (0.0, 0.5, 0.0) in the $P4/mbm$ phase, the Pb atoms at 4c site (0.5, 0.5, 0.0) in the $I4/mcm$ transform to 2b site (0.0, 0.0, 0.5) in the $P4/mbm$ phase, and the I atoms at the 4a and 8h positions [(0.5, 0.5, 0.75), (0.193, 0.693, 0.0)] in the $I4/mcm$ phase transform to 2a and 4h positions [(0.0, 0.0, 0.0), (0.193, 0.306, 0.5)] in the $P4/mbm$ phase, respectively. We found the total energy of $Imm2$ is lower than that of $P4/mbm$, which may be driving phase transition from $P4/mbm$ to lower symmetry $Imm2$ structure under pressure. In addition, by comparing the atomic coordinates of the two structures, we found that the coordinates of Fr and Pb atoms are almost unchanged. The $P4/mbm$ structure transform to $Imm2$ owing to the displacement of iodine atom [e.g., (0.657, 0.980, 0.984)→(0.718, 0.984, 0.712); (0.157, 0.480, 0.734)→(0.232, 0.484, 0.600); (0.303, 0.980, 0.734)→(0.250, 0.984, 0.712); (0.803, 0.480, 0.734)→(0.735, 0.484, 0.600), etc.].

Guided by this insight from the case of $FrPbI_3$, we can discuss the tentative phase transition behavior of $MAPbI_3$ under pressure. Due to the incorporation of nonspherical MA molecule, the inorganic octahedral unit of $MAPbI_3$ would distort and tilt along three crystallographic axes. The experimentally determined structures under pressure are cubic ($Im\bar{3}$) and orthorhombic ($Imm2$) [22–26,28]. Since the cubic phase has the highest energy among all 14 distorted structures [Fig. 2(a)], we do not anticipate its formation under hydrostatic pressure. In addition, we found that the orthorhombic $Imm2$ structure and tetragonal $P4/mbm$ structure exhibit the same tilt pattern ($a^0a^0c^+$). We propose that $P4/mbm$ is an intermediate phase. Figure 5(a) shows the pressure dependence of ΔH of $P4/mbm$ and $Imm2$ relative to $I4/mcm$ structure for $MAPbI_3$ with all MA molecules orientated to the [111] direction. Although spin-orbit coupling (SOC) impacts electronic properties, structural parameters including the trend in ΔH are consistent with PBE without SOC, as shown in Fig. 5(b). The pressure dependence of ΔH corresponding to [100] and [110] orientations are shown in Figs. S9a and S9b [33], respectively. We find that the $I4/mcm$ structure is the most stable phase up to about 0.25 GPa. Upon further compression, the $P4/mbm$ and $Imm2$ structures become more energetically stable. According to Fig. 5(a), $Imm2$ structure is lower in energy than $P4/mbm$. At room temperature, MA cations are expected to be disordered in the bulk. Still, there may be some preferential reorientations that impact H bonding and stabilization of a particular phase under pressure. Nevertheless, trends from $FrPbI_3$ (Figs. 2–4) and Fig. 5(a) results indicate that interplay between octahedral tilting and bond compression may be driving the $MAPbI_3$ phase transition under pressure with MA orientation playing a lesser role. Based on the above analysis,

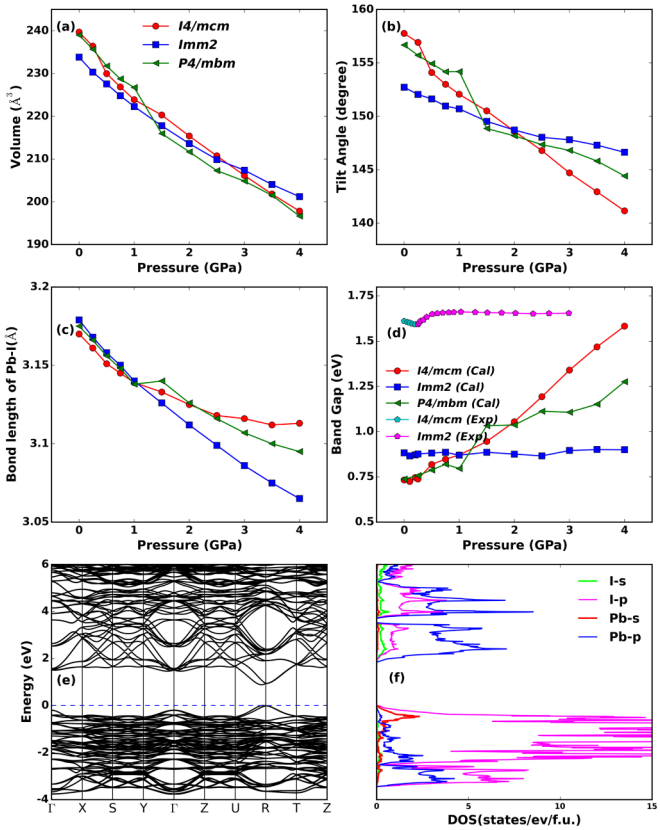

FIG. 6. (a)–(d) The volume variation, Pb-I-Pb bending angle of adjacent octahedral layer, Pb-I bond length, calculated and experimental band gaps of tetragonal (*I4/mcm*, *P4/mbm*) structure and orthorhombic *Imm2* structure of $MAPbI_3$ as a function of pressure [28]. (e), (f) The calculated band structures and density of states of orthorhombic *Imm2* structure of $MAPbI_3$ at 0.5 GPa using the DFT-PBE method. The coordinates of high-symmetry K points are Γ (0, 0, 0), X (0.5, 0, 0), S (0.5, 0.5, 0), Y (0, 0.5, 0), Z (0, 0, 0.5), U (0.5, 0, 0.5), R (0.5, 0.5, 0.5), T (0, 0.5, 0.5).

we propose the phase transition pathway of $MAPbI_3$ structure is a two-step process from *I4/mcm*→ *P4/mbm*→ *Imm2* with the appearance of in-phase rotations of the PbI_6 octahedral network along the c axis. The tetragonal *P4/mbm* structure serves as an intermediate phase. We also simulated the x-ray diffraction (XRD) patterns of tetragonal β phase (*I4/mcm*) and orthorhombic phase (*Fmmm*) as shown in Fig. S10 [33] . Both of them agree well with the experimental XRD at atmospheric pressure because of the high similarity between the two structures. However, we found that the calculated total energy of the tetragonal β phase is 55 meV/f.u. lower than that of the orthorhombic phase. It means that the tetragonal phase is the ground-state structure, which is consistent with the crystallographic information in most experiments [25]. Therefore, the tetragonal structure (*I4/mcm*) is chosen as the starting phase.

We subsequently investigated the structural and electronic properties of $MAPbI_3$ tetragonal (*I4/mcm*, *P4/mbm*) and orthorhombic (*Imm2*) phases under compression. Figure 6(a) shows variation in the unit-cell volume as a function of pressure. The volume contraction is closely associated to changes in the Pb-I-Pb bending angle and Pb-I bond length. For *I4/mcm* phase, the Pb-I-Pb bond angle decreases faster and Pb-I bond length shrinks slower with pressure compared to the tetragonal *P4/mbm* and orthorhombic *Imm2* phases [Figs. 6(b) and 6(c)]. The reduction of Pb-I-Pb bending angle is the main reason for volume reduction in the tetragonal structure, while Pb-I bond contraction is mostly responsible in the orthorhombic structure. While the volume of orthorhombic phase decreases gradually with increasing pressure, that of the tetragonal phase undergoes an abrupt reduction between 0.25–0.5 GPa [Fig. 6(a)]. Notice a similar discontinuity in its Pb-I-Pb bending angle [Fig. 6(b)], which is consistent with pressure-induced structural modification approximately in the pressure range 0.25–0.5 GPa [25,28]. Figure 6(d) shows pressure dependence of the band gap of tetragonal and orthorhombic structures. The calculated band gaps along with Pb-I-Pb bending angle and Pb-I bond length are shown in Tables S4 and S5 [33]. At ambient pressure, the calculated gap of the tetragonal phase is 1.58 eV (0.73 eV with SOC as shown in Figs. S11 and S12 [33]), which is close to the measured band gap in experiments [27]. Here, it is important to note that the surprising agreement between PBE calculated and experimental band gap of $MAPbI_3$ is a happy coincidence due to systematic error cancellation. Including spin-orbit effect will indeed lead to underestimated band gaps as shown in Fig. S12a [33]. With pressure, the band gaps of *I4/mcm* structure decrease before 0.25 GPa and then gradually increase. This is consistent with the experimental trend before 0.25 GPa. In experiment, the phase transition began at 0.25 GPa and completely finished until 1 GPa. Upon the phase transition completed, the band gaps decrease slightly with the increase of pressure. The evolution of calculated band gaps under high pressure is consistent with experimental photoluminescence (PL) shift [25,28]. The band-gap variation under pressure can also be understood from band-structure characteristics of $MAPbI_3$. The band-gap reduction of *I4/mcm* is mainly ascribed to the shrinking Pb-I bond at the beginning of the loading pressure. It is consistent with the redshift phenomenon in the PL spectrum within 0.3 GPa [25]. Beyond this pressure, an abrupt increase in the octahedral tilting [reduction of Pb-I-Pb bending angle in *I4/mcm*, Fig. 6(b)] is indicative of structural modification. It is responsible for the PL blueshift observed above 0.3 GPa [25], where larger octahedral tilting reduces orbital overlap (as shown in Fig. S13 [33]) and increases band gap of the *I4/mcm* phase. The band gaps of *P4/mbm* phase undergoes three stages of changes with pressure: first increase (before 0.75 GPa), then rapidly decrease (0.75 $\sim$ 1.0 GPa), and finally slowly increase (above 1.0 GPa). The increase of band gaps is mainly caused by the enlargement in octahedral tilting. Once the high-pressure transformation to the orthorhombic *Imm2* structure is complete, the competing effects Pb-I bond contraction and Pb-I-Pb bending lead to a continuous, albeit slow, decrease in the band gap, which is again consistent with PL redshift in that pressure range [see *Imm2* band gaps in Fig. 6(d)] [25]. The understanding of band-gap reduction of orthorhombic *Imm2* structure under compression can be elucidated by considering the band nature. The calculated electronic band structure and density of states (DOS) of orthorhombic *Imm2* structure of $MAPbI_3$ at 0.5 GPa are shown in Figs. 6(e) and 6(f). The band gap is determined by the VBM (valence band maximum)

and CBM (conduction band minimum) position. As shown in Fig. 6(e), the VBM is mainly composed of the antibonding hybridized states between Pb 6*s* and I 5*p* orbitals, whereas the CBM has mostly a nonbonding Pb 6*p* orbital. As the pressure increases, the decrease of bond length of Pb-I contributes to the enhanced coupling of Pb *s* and I *p* orbitals. The enhanced coupling will push up the VBM, whereas the CBM is not sensitive to the change of bond length. As a result, the band gap decreases until 2.5 GPa. As the pressure increases, the rotation of MA cations is hindered, and their dipole moments become directional [55,56]. The increased octahedral distortion and tilting at high pressure would lead to the slight band-gap increase when pressure is above 2.5 GPa [57]. Finally, we looked at a pressure-dependent variation of I-Pb-I angle which is linked to distortions within an octahedron (as opposed to Pb-I-Pb bending angles that are linked to octahedral tilting). The I-Pb-I angle decreases continuously with pressure in *I*4/*mcm* phase of $MAPbI_3$ as shown in Fig. S14 [33]. It is interesting that the I-Pb-I angles in the *Imm2* phase remain almost unchanged until a pressure of about 2 GPa (Fig. S14 [33]), when it undergoes a sharp decrease. It indicates a modest octahedral distortion occurring about this pressure. Also, notice that the other pressure-dependent parameters of *Imm2* phase depicted in Figs. 6(a)–6(c) do not show abrupt behavior. We surmise that octahedral distortion and subsequent changes in orbital overlap between I and Pb states may be driving the band-gap variation seen around 2–3 GPa in the *Imm2* phase [Fig. 6(d)].

IV. CONCLUSIONS

To summarize, pressure-induced phase transition behavior of $MAPbI_3$ is proposed in the 0–3 GPa range. Substituting Fr in place of the rotationally disordered MA cation, we investigated a comprehensive list of 14 distorted $FrPbI_3$ systems derived from the cubic $Pm\bar{3}m$ structure. The stability of the tilt systems is analyzed via harmonic and finite-temperature anharmonic phonon spectra, while (static) energetic calculations provide trends among the different phases with pressure. We show that $FrPbI_3$, under pressure, tends to transform from $I4/mcm \rightarrow P4/mbm$ with the appearance of in-phase rotations of the PbI_6 octahedral network along the crystallographic *c* axis. Based upon these $FrPbI_3$ trends and subsequent calculations with tetragonal and orthorhombic $MAPbI_3$, we propose its pressure-induced transition: $I4/mcm \rightarrow P4/mbm \rightarrow Imm2$, with *P*4/*mbm* serving as an intermediate phase. Discontinuity in the calculated cell volume and Pb-I-Pb bending angle of *I*4/*mcm* phase around 0.25–0.5 GPa are consistent with the proposed phase transition. Furthermore, agreement between observed PL shifts and estimated band-gap variations in $MAPbI_3$ confirm a tetragonal to orthorhombic phase transition under high pressure and ambient temperature conditions. Trends from $FrPbI_3$ point towards dynamical fluctuations in the inorganic lattice at finite temperature and its important role in phase stabilization.

ACKNOWLEDGMENTS

The authors acknowledge funding support from National Natural Science Foundation of China under Grant No. 12004131, the China Postdoctoral Science Foundation under Grant No. 2018M642766, Jilin Province Science and Technology Development Program under Grant No. 20190201016JC. Calculations were performed in part at the high performance computing center of Jilin University and Henan Supercomputer Center.

[1] A. Kojima, K. Teshima, Y. Shirai, and T. Miyasaka, J. Am. Chem. Soc. **131**, 6050 (2009).
[2] https://www.nrel.gov/pv/assets/pdfs/best-research-cell-efficiencies.20190802.pdf.
[3] X. Jia, C. Zuo, S. Tao, K. Sun, Y. Zhao, S. Yang, M. Cheng, M. Wang, Y. Yuan, J. Yang, F. Gao, G. Xing, Z. Wei, L. Zhang, H.-L. Yip, M. Liu, Q. Shen, L. Yin, L. Han, S. Liu *et al.*, Sci. Bull. **64**, 1532 (2019).
[4] Z. Xiao and Y. Yan, Adv. Energy Mater. **7**, 1701136 (2017).
[5] W.-J. Yin, J.-H. Yang, J. Kang, Y. Yan, and S.-H. Wei, J. Mater. Chem. A **3**, 8926 (2015).
[6] A. Walsh, D. O. Scanlon, S. Chen, X. G. Gong, and S.-H. Wei, Angew. Chem. Int. Ed. **54**, 1791 (2015).
[7] Q. Dong, Y. Fang, Y. Shao, P. Mulligan, J. Qiu, L. Cao, and J. Huang, Science **347**, 967 (2015).
[8] S. D. Stranks, G. E. Eperon, G. Grancini, C. Menelaou, M. J. P. Alcocer, T. Leijtens, L. M. Herz, A. Petrozza, and H. J. Snaith, Science **342**, 341 (2013).
[9] D. Zhao, Y. Yu, C. Wang, W. Liao, N. Shrestha, C. R. Grice, A. J. Cimaroli, L. Guan, R. J. Ellingson, K. Zhu, X. Zhao, R.-G. Xiong, and Y. Yan, Nat. Energy **2**, 17018 (2017).
[10] G. Na and L. Zhang, Light: Sci. Appl. **9**, 106 (2020).
[11] N. J. Jeon, J. H. Noh, Y. C. Kim, W. S. Yang, S. Ryu, and S. I. Seok, Nat. Mater. **13**, 897 (2014).
[12] D. Liu and T. L. Kelly, Nat. Photonics **8**, 133 (2014).
[13] Q. Chen, H. Zhou, Z. Hong, S. Luo, H.-S. Duan, H.-H. Wang, Y. Liu, G. Li, and Y. Yang, J. Am. Chem. Soc. **136**, 622 (2014).
[14] A. Amat, E. Mosconi, E. Ronca, C. Quarti, P. Umari, M. K. Nazeeruddin, M. Grätzel, and F. De Angelis, Nano Lett. **14**, 3608 (2014).
[15] W.-J. Yin, T. Shi, and Y. Yan, Appl. Phys. Lett. **104**, 063903 (2014).
[16] Z. Liu, G. Na, F. Tian, L. Yu, J. Li, and L. Zhang, InfoMat **2**, 879 (2020).
[17] S. Luo, T. Li, X. Wang, M. Faizan, and L. Zhang, WIREs Computat. Mol. Sci. **11**, e1489 (2021).
[18] X. Wang, Y. Fu, G. Na, H. Li, and L. Zheng, Acta Phys. Sin. **68**, 157101 (2019).
[19] C.-X. Zhang, T. Shen, D. Guo, L.-M. Tang, K. Yang, and H.-X. Deng, InfoMat **2**, 1034 (2020).
[20] L. Zhang, Y. Wang, J. Lv, and Y. Ma, Nat. Rev. Mater. **2**, 17005 (2017).
[21] Z. Ma, Z. Liu, S. Lu, L. Wang, X. Feng, D. Yang, K. Wang, G. Xiao, L. Zhang, S. A. T. Redfern, and B. Zou, Nat. Commun. **9**, 4506 (2018).
[22] A. Jaffe, Y. Lin, C. M. Beavers, J. Voss, W. L. Mao, and H. I. Karunadasa, ACS Central Sci. **2**, 201 (2016).
[23] M. Szafrański and A. Katrusiak, J. Phys. Chem. Lett. **7**, 3458 (2016).

[24] S. Jiang, Y. Fang, R. Li, H. Xiao, J. Crowley, C. Wang, T. J. White, W. A. Goddard, Z. Wang, T. Baikie, and J. Fang, Angew. Chem., Int. Ed. **55**, 6540 (2016).
[25] L. Kong, G. Liu, J. Gong, Q. Hu, R. D. Schaller, P. Dera, D. Zhang, Z. Liu, W. Yang, K. Zhu, Y. Tang, C. Wang, S.-H. Wei, T. Xu, and H.-k. Mao, Proc. Natl. Acad. Sci. USA **113**, 8910 (2016).
[26] F. Capitani, C. Marini, S. Caramazza, P. Postorino, G. Garbarino, M. Hanfland, A. Pisanu, P. Quadrelli, and L. Malavasi, J. Appl. Phys. **119**, 185901 (2016).
[27] C. C. Stoumpos, C. D. Malliakas, and M. G. Kanatzidis, Inorg. Chem. **52**, 9019 (2013).
[28] H. Guo, R. Liu, L. Wang, J. Cui, B. Song, K. Wang, B. Liu, and B. Zou, Acta Phys. Sin. **66**, 30701 (2017).
[29] G. Kresse and J. Furthmüller, Phys. Rev. B **54**, 11169 (1996).
[30] G. Kresse and J. Furthmüller, Comput. Mater. Sci. **6**, 15 (1996).
[31] P. E. Blöchl, Phys. Rev. B **50**, 17953 (1994).
[32] J. P. Perdew, K. Burke, and M. Ernzerhof, Phys. Rev. Lett. **77**, 3865 (1996).
[33] See Supplemental Material at http://link.aps.org/supplemental/10.1103/PhysRevMaterials.5.054603, which includes Refs. [25,53,55] for details of experimental lattice constants and fraction coordinates of high-symmetry K points.
[34] J. Klimeš, D. R. Bowler, and A. Michaelides, J. Phys.: Condens. Matter **22**, 022201 (2010).
[35] P. Fu, S. Hu, J. Tang, and Z. Xiao, Front. Optoelectron. (2021), doi:10.1007/s12200-021-1227-z.
[36] A. Togo and I. Tanaka, Scr. Mater. **108**, 1 (2015).
[37] O. Hellman, I. A. Abrikosov, and S. I. Simak, Phys. Rev. B **84**, 180301(R) (2011).
[38] O. Hellman, P. Steneteg, I. A. Abrikosov, and S. I. Simak, Phys. Rev. B **87**, 104111 (2013).
[39] O. Hellman and I. A. Abrikosov, Phys. Rev. B **88**, 144301 (2013).
[40] G. Henkelman, B. P. Uberuaga, and H. Jónsson, J. Chem. Phys. **113**, 9901 (2000).
[41] C. J. Howard and H. T. Stokes, Acta Crystallogr., Sect. B **54**, 782 (1998).
[42] X.-G. Zhao, D. Yang, J.-C. Ren, Y. Sun, Z. Xiao, and L. Zhang, Joule **2**, 1662 (2018).
[43] A. M. A. Leguy, J. M. Frost, A. P. McMahon, V. G. Sakai, W. Kockelmann, C. Law, X. Li, F. Foglia, A. Walsh, B. C. O'Regan, J. Nelson, J. T. Cabral, and P. R. F. Barnes, Nat. Commun. **6**, 7124 (2015).
[44] Q. Xu, A. Stroppa, J. Lv, X. Zhao, D. Yang, K. Biswas, and L. Zhang, Phys. Rev. Mater. **3**, 125401 (2019).
[45] X.-G. Wang, D. Yang, Y. Sun, T. Li, L. Zhang, L. Yu, and A Zunger, J. Am. Chem. Soc. **139**, 6718 (2017).
[46] W. A. Saidi and J. J. Choi, J. Chem. Phys. **145**, 144702 (2016).
[47] G. Volonakis, A. A. Haghighirad, H. J. Snaith, and F. Giustino, J. Phys. Chem. Lett. **8**, 3917 (2017).
[48] A. D. Wright, C. Verdi, R. L. Milot, G. E. Eperon, M. A. Pérez-Osorio, H. J. Snaith, F. Giustino, M. B. Johnston, and L. M. Herz, Nat. Commun. **7**, 11755 (2016).
[49] K. T. Butler, J. Mater. Chem. C **6**, 12045 (2018).
[50] M. A. Pérez-Osorio, A. Champagne, M. Zacharias, G.-M. Rignanese, and F. Giustino, J. Phys. Chem. C **121**, 18459 (2017).
[51] C. E. Patrick, K. W. Jacobsen, and K. S. Thygesen, Phys. Rev. B **92**, 201205(R) (2015).
[52] L.-y. Huang and W. R. L. Lambrecht, Phys. Rev. B **90**, 195201 (2014).
[53] W. Setyawan and S. Curtarolo, Comput. Mater. Sci. **49**, 299 (2010).
[54] H. T. Stokes and D. M. Hatch, *Isotropy Subgroups of the 230 Crystallographic Space Groups* (World Scientific, Singapore, 1988).
[55] D. Yang, J. Lv, X. Zhao, Q. Xu, Y. Fu, Y. Zhan, A. Zunger, and L. Zhang, Chem. Mater. **29**, 524 (2017).
[56] Q. Xu, D. Yang, J. Lv, Y. Sun, and L. Zhang, Small Methods **2**, 1700316 (2018).
[57] X. Lü, W. Yang, Q. Jia, and H. Xu, Chem. Sci. **8**, 6764 (2017).